Catalysis Science & Technology

PAPER

View Article Online
View Journal | View Issue

Cite this: *Catal. Sci. Technol.*, 2016, 6, 6806

Towards stable single-atom catalysts: strong binding of atomically dispersed transition metals on the surface of nanostructured ceria†

Alberto Figueroba,[a] Gábor Kovács,[a] Albert Bruix[b] and Konstantin M. Neyman*[ac]

The interaction of a series of different transition metal atoms with nanoparticulate CeO_2 has been studied by means of density-functional calculations. Recently, we demonstrated the ability of sites exposed on {100} nanofacets of CeO_2 to very strongly anchor atomic Pt, making the formed species exceptionally efficient single-atom anode catalysts for proton-exchange membrane fuel cells. Herein, we analyzed the capacity of these surface sites to accommodate all other group VIII–XI transition metal atoms M = Fe, Ru, Os, Co, Rh, Ir, Ni, Pd, Cu, Ag, and Au. The interaction of the M atoms with {100} nanofacets of ceria leads to oxidation of the former and such interaction is calculated to be stronger than the binding of the atoms in the corresponding metal nanoparticles. Comparing the stability of metal–metal and metal-oxide bonds allows one to establish which metals would more strongly resist agglomeration and hence allows the proposal of promising candidates for the design of single-atom catalysts. Indeed, the remarkable stability of these adsorption complexes (particularly for Pt, Pd, Ni, Fe, Co, and Os) strongly suggests that atomically dispersed transition metals anchored as cations on {100} facets of nanostructured ceria are stable against agglomeration into metal particles. Therefore, these sites appear to be of immediate relevance to the preparation of stable catalysts featuring the highest possible metal efficiency in nanocatalysis.

Received 6th February 2016,
Accepted 26th February 2016

DOI: 10.1039/c6cy00294c

www.rsc.org/catalysis

1. Introduction

Reducing the amount of precious noble metals used in catalytic materials is one of the challenges in catalysis research.[1] The ever-increasing demand from the automobile industry along with limited supply has a critical effect on the price of such metals, which is an obstacle for the large-scale implementation of applications that require noble-metal-based catalysts.[2–4] It is well known, for example, that the very high cost of platinum is one of the stringent factors limiting the wider use of fuel cell technology.[3,4]

Two strategies are commonly followed to cope with the challenge of reducing the content of precious metals in catalysts. The first strategy involves the partial or complete replacement of the precious metal by less-expensive materials. Following it, numerous alternatives have been proposed that can substantially decrease the cost of the catalyst.[5–7] However, the resulting catalytic performance is often inferior to that of the analogous noble-metal systems. The other strategy focuses on the more efficient utilization of the noble metal rather than its substitution. This approach aims to maximize the specific catalytic performance of the noble-metal phase, *i.e.* its per-atom activity. The latter has been customarily achieved by finely dispersing the metal on supports – a paradigm of nanocatalysis.[8,9]

The limiting case of metal dispersion corresponds to catalytic systems with atomic metal species on the surface of the support, denoted as single-atom catalysts (SACs).[10–12] Notably, non-reducible metal-oxide supports exposing regular surfaces, such as MgO(100),[13] adsorb atomic transition metal species too weakly to prevent their clustering. A similar situation takes place on the most stable (111) surface of CeO_2, a reducible oxide support widely used in catalysis.[14] This indicates that the formation of transition metal SACs that are sufficiently stable to counteract metal–metal bond formation upon sintering requires special strongly binding sites on the supports.

Various composites featuring atomically dispersed noble metals have been reported to be catalytically active for different reactions. For instance, cationic Pt and Au species on nanostructured ceria[15] and more inert oxides, such as zeolites and silica,[16,17] were found to catalyze the water-gas shift

---

[a] *Departament de Química Física & Institut de Química Teòrica i Computacional, Universitat de Barcelona, C/Martí i Franquès 1, 08028 Barcelona, Spain*
[b] *Interdisciplinary Nanoscience Center (iNANO) and Department of Physics and Astronomy, Aarhus University, DK-8000 Aarhus C, Denmark*
[c] *Institució Catalana de Recerca i Estudis Avançats (ICREA), 08010 Barcelona, Spain. E-mail: konstantin.neyman@icrea.cat*

† Electronic supplementary information (ESI) available: Selected calculated structural data of M_1–$Ce_{40}O_{80}$ models, experimental cohesive energies of the considered metals M and heats of formation of their most stable oxides. See DOI: 10.1039/c6cy00294c

reaction at low temperatures. Materials formed by Pd cations anchored on alumina[18] and Pt cations on FeO_x (ref. 19) were reported to be active towards CO oxidation. High catalytic hydrogenation activity has also been attributed to such SACs, as for instance Pd atoms anchored to cavities of mesoporous graphitic carbon nitride[20] and FeO_x-supported Pt.[21] These and analogous systems represent a promising new generation of cost-effective catalytic materials. Most publications point to oxidized states of the supported noble-metal atoms as the active species in these catalysts. It should be noted, however, that the structure of SAC materials can change under the often harsh catalytic conditions, leading to partial loss of the specific activity of the metal due to its sintering or bulk diffusion. These phenomena can strongly reduce the number of active metal sites exposed to reactants. Thus, it is essential that the support provides sufficient concentration of surface sites that can anchor the metal atoms strongly enough to prevent agglomeration and bulk diffusion. To this end, {100} nanofacets of ceria nanoparticles (NPs) have been shown to be remarkably efficient in anchoring single Pt atoms as Pt^{2+} cations.[22,23] Density-functional calculations combined with X-ray photoemission spectroscopy (XPS) experiments were used to determine that Pt^{2+} cations adsorbed on such sites are efficiently protected from reduction, aggregation or diffusion into the bulk, up to high temperatures.[22] This specific nanofacet site thus fulfills the stability requirements for a SAC. Importantly, this surface site consisting of four O atoms in a square-planar geometry (below referred to as an O_4 site), is not unique to ceria NPs. This structural motif can also be found on extended $CeO_2(100)$ surfaces[24] and on the step edges of low-energy $CeO_2(111)$ islands.[25]

The extraordinary stability of Pt atoms on CeO_2 {100} nanofacets suggests that these sites may also strongly bind other transition metal atoms. To assess this peculiar binding propensity important for preparing stable SACs, we have investigated the interaction of these sites with transition metal atoms M = Fe, Ru, Os, Co, Rh, Ir, Ni, Pd, Cu, Ag, and Au in groups VIII–XI of the periodic table. Our results reveal that the O_4 sites on {100} facets of ceria NPs strongly bind and oxidize single atoms of all studied metals. Comparison of the adsorption energies of the M_1 species with the binding energies of the corresponding atoms in metal NPs indicates high energetic stability of the anchored M_1 species against agglomeration. The oxide support acts in the anchoring according to coordination chemistry principles – as a polydentate ligand formed by surface oxygen anions.[26] This explains how the adsorption bonds are as strong as metal–ligand bonds in common transition metal complexes. Findings of the present study suggest general guidelines for the preparation of enduring transition metal SACs.

2. Computational details

The adsorption of single atoms of 11 different transition metals on the {100} O_4 site of a ceria NP has been investigated by means of periodic spin-polarized density-functional calculations. The generalized gradient approach (GGA) corrected with the on-site Coulomb interaction Hubbard term U (GGA+U) has been used.[27–29] Common exchange-correlation potentials suffer from an incomplete cancellation of the self-interaction error, thus leading to a poor description of strongly correlated systems. The U-correction scheme offers a computationally feasible improvement, which enables an appropriate treatment of transition and rare-earth metal oxides featuring localized electrons in d and f orbitals, respectively. The GGA+U approach has been widely used to describe ceria-based systems, whose Ce 4f states can be occupied upon reduction.[30] However, there is no unique U value allowing simultaneous reproduction of all properties of oxidized and reduced ceria.[31] For example, calculations with larger values of U predict band gaps in better agreement with experiment, but overestimate interatomic distances in ceria. Following previous studies of ceria NPs,[32–35] present calculations have been performed using the PW91 (ref. 36) exchange-correlation potential corrected with a value of U = 4 eV (referred to as the PW91+4 scheme). The effect of using different U values on the calculated properties was assessed (see section 4).

Calculations have been carried out using the VASP code,[37–39] representing the valence states in plane-wave basis sets with a cut-off of 415 eV for the kinetic energy. The core–valence interaction has been described through the projector augmented wave method.[40] Only the Γ-point has been used to sample the reciprocal space. The electron density was self-consistently converged with a 10^{-4} eV total energy threshold and all geometric structures were optimized until forces acting on each atom became smaller than 0.02 eV $Å^{-1}$. Some adsorbed metal atoms can exhibit different oxidation states. This has been explored and the resulting oxidation states of the adsorbed M_1 species have been determined by the analysis of the localized magnetic moments on Ce cations. Bader charge analysis[41] has also been performed.

3. M_1–CeO_2 and M_n models

A cuboctahedral $Ce_{40}O_{80}$ NP (Fig. 1) has been chosen as a representative model of nanostructured CeO_2, previously shown to be capable of reproducing various experimental observations[22,32,35] (effect of the NP size on the calculated observations is briefly addressed in section 4). The structure of this NP resulted from a global optimization using interionic potential and density-functional calculations.[33,34] The $Ce_{40}O_{80}$ NP retains the cubic fluorite-type crystallinity of bulk CeO_2 and exposes small O-terminated {111} and {100} facets. The latter corresponds to the polar (100) surface, less stable than the (111) surface.[42] Yet, ceria nanosystems with abundant [100] terminations have also been prepared, ranging from nanocrystals with extended (100) terraces[24] to nanocubes exposing only {100} facets.[43] The size of the periodically repeated unit cell was chosen to keep distances between NPs in neighboring cells ≥700 pm to avoid significant spurious interactions of the NPs.

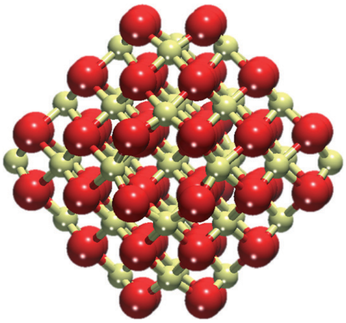

Fig. 1 Cuboctahedral $Ce_{40}O_{80}$ nanoparticle model of nanostructured ceria. Yellow and red spheres represent Ce^{4+} cations and O^{2-} anions, respectively.

The adsorption energies, E_{ad}, of a metal atom M on the ceria NP were calculated as $E_{ad} = E(M_1\text{–}Ce_{40}O_{80}) - E(M_1) - E(Ce_{40}O_{80})$, where $E(M_1)$ is the total ground-state energy of an isolated metal atom and $E(M_1\text{–}Ce_{40}O_{80})$ and $E(Ce_{40}O_{80})$ are the total energies of the ceria NP with and without the adsorbed metal atom, respectively. Negative adsorption energy values correspond to stabilizing interactions with respect to the separated M_1 and $Ce_{40}O_{80}$ fragments. In order to compare the strength of this interaction with that of M_1 agglomeration into metal particles M_n, we have calculated the binding energy, E_{ad79}, of an edge M atom in the M_{79} model (a bulk cut of the *fcc* crystal, Fig. 2) as $E_{ad79} = E(M_{79}) - E(M_1) - E(M_{78})$. Similarly, the propensity of the anchored M_1 species to agglomerate can be assessed by comparing the E_{ad} values with the experimental metal cohesive energies (see Table S1†).

4. Results and discussion

We performed a comparative study of the adsorption of 3d (Fe, Co, Ni, Cu), 4d (Ru, Rh, Pd, Ag) and 5d (Os, Ir, Pt,[22] Au) metal atoms on O_4 sites of {100} nanofacets of the $Ce_{40}O_{80}$ NP. This is not the only site on the NP where metal atoms can be anchored, but the adsorption of Pt on other NP sites was calculated to be much weaker than on the O_4 site[22,23] and similar in strength to the adsorption on $CeO_2(111)$ surfaces.[44] Since this site preference is expected for the adsorption of all metal atoms under scrutiny, we focused on interactions with the O_4 site.

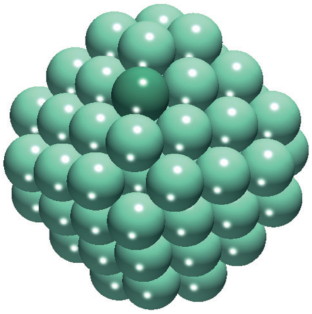

Fig. 2 Model M_{79} NP used for estimating the binding energy of atoms in metal particles. The darker green M atom in the edge position was removed for calculating its binding energy to the remaining M_{78} species.

The optimized structures for the $M_1\text{–}Ce_{40}O_{80}$ systems are shown in Fig. 3. *Via* the analysis of spin moments, we were able to quantify the charge transfer taking place upon atom deposition on the {100} nanofacet. Such charge transfer results in the oxidation of the M_1 adsorbate with the concomitant reduction of a certain number of Ce^{4+} cations to Ce^{3+}. The number of reduced Ce cations depends on the M atom and equals its oxidation state. Corner Ce^{4+} cations in the $Ce_{40}O_{80}$ NP are the easiest to reduce due to their lower coordination number and an accordingly less destabilizing electrostatic environment.[34,45] These corner Ce^{4+} cations accepted electrons from M atoms, which were concomitantly oxidized to +1 or +2 oxidation states. In oxidation states higher than +2, a search for the most stable locations of the additionally formed Ce^{3+} cations has not been performed in view of a very high number of possible configurations. The location of the Ce^{3+} cations in less stable positions of the NP could induce a destabilization of the adsorption by up to 40 kJ mol^{-1} per Ce^{3+} cation.[34] Yet, this difference does not affect the upcoming discussion of the adsorption energy values of M atoms. Note that the appearance of Ce^{3+} cations (larger than Ce^{4+}) significantly elongates the corresponding Ce–O distances, to 228 pm from 213 pm in the pristine CeO_2 NP (see Fig. S1 and S2†).

Herein, we discuss the oxidation states for each adsorbed metal atom and the M–O coordination modes (see for details Fig. S1 and S2†). We also comment on how our results compare to pertinent experimental data.

Group VIII metals

Adsorbed atoms of group VIII feature different oxidation states, +3 – Fe and Ru, and +6 – Os. Two Ce^{3+} cations are located in the corner positions, whereas additional f electrons are found in other surface Ce positions close to the occupied {100} site. Single M atoms bind to oxygen atoms of the O_4 site in a square-planar fashion. The nearest M–O distances are 184–187 pm for Fe, 196–199 pm for Ru and 184–185 pm for Os (see Fig. S1†), much shorter than the *ca.* 225 pm distance between the O atoms and the center of the O_4 moiety in the pristine $Ce_{40}O_{80}$ NP.[22] A similar coordination mode of Fe was detected by Mössbauer spectroscopy for Fe^{3+} cations inserted into the lattice of ceria–zirconia catalysts.[46] In turn, the self-dispersion of Ru metal powder on ceria in the form of small particles and single atoms in a highly oxidized state was demonstrated to be very stable by X-ray absorption near edge structure (XANES) and Raman spectroscopic techniques.[47]

Group IX metals

Atoms of this group manifested more diverse oxidation states. Co is the only metal atom in this group that features a +3 state. Despite the well-known stability of the +3 state for

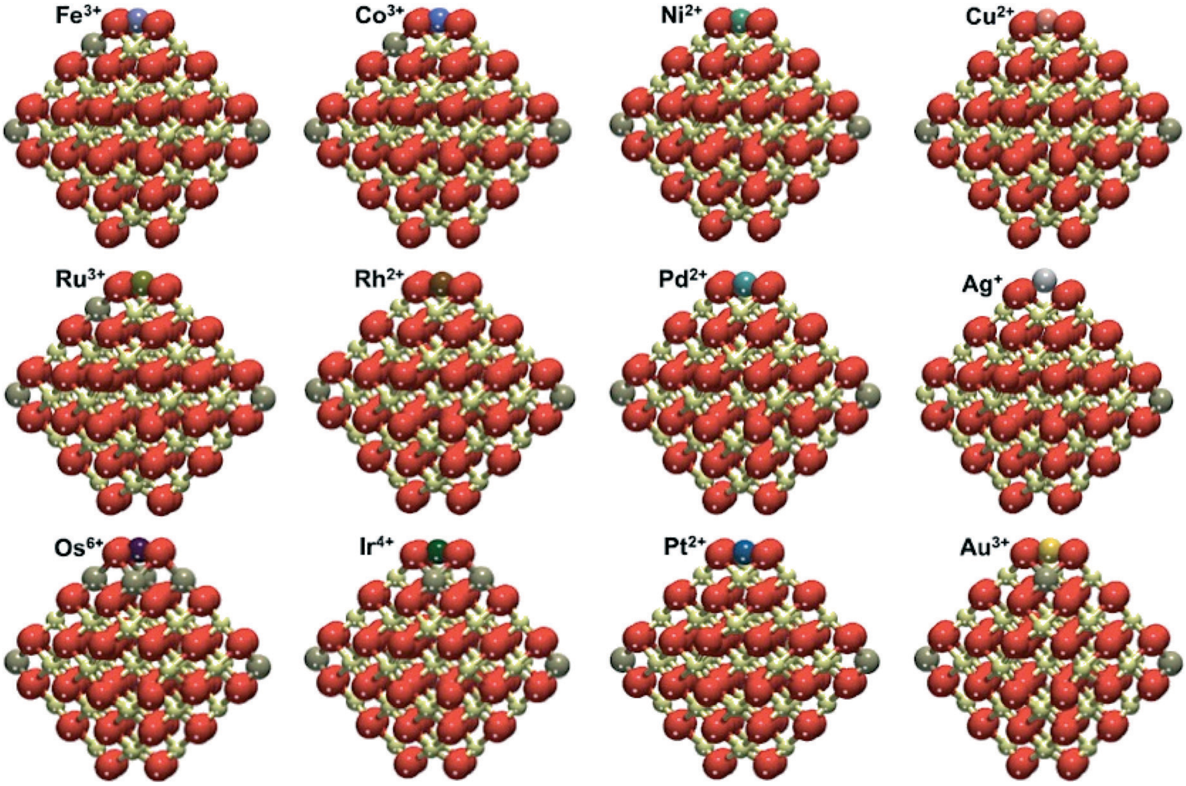

Fig. 3 Overview of the M_1–$Ce_{40}O_{80}$ structures calculated for the adsorption of different transition metal atoms (M) on the {100} facet of the $Ce_{40}O_{80}$ nanoparticle. Yellow, brown and red spheres represent Ce^{4+}, Ce^{3+} and O^{2-} ions, respectively. See selected calculated interatomic distances in Fig. S1 and S2.†

Rh, we calculated it to be adsorbed only in the +2 state. Similar to group VIII, only the 5d element Ir undergoes further oxidation to the +4 state. Just as for adsorbed group VIII atoms, Ce^{3+} cations are formed in NP corners and close to the O_4 site occupied by M. Co and Ir are bound in a square-planar coordination mode with M–O distances 185–186 pm for Co and 192–197 pm for Ir. Differently, Rh^{2+} appears to prefer linear coordination with two short (198 pm) and two long distances (208 pm). Such group IX cationic species have been identified experimentally on ceria-based materials. Co^{3+} cations were detected using temperature-programmed reduction (TPR) and XPS experiments in ceria–zirconia catalysts.[48] Rh^{2+} cations were evidenced on ceria–zirconia mixed oxides by Fourier transform infrared (FTIR) spectroscopy.[49] Finally, surface Ir^{4+} species were identified in ceria by TPR and diffuse reflectance infrared Fourier transform spectroscopy (DRIFTS).[50]

Group X metals

Group X atoms Ni and Pd are calculated to be adsorbed similarly to Pt as +2 cations, coordinated in a square-planar mode, very characteristic of d^8 metal centers of this group. The interatomic M–O distances are 189 pm for Ni and 205 pm for both Pd and Pt. The same oxidation state was recently reported for Ni^{2+} on defect sites of the $CeO_2(111)$ surface.[51] It was shown that the interaction of Pd with ceria can lead to the formation of Pd–O–Ce surface superstructures featuring Pd^{2+} cations and active in catalytic combustion of methane.[52] There is experimental evidence that Pd^{2+} cations in the square-planar coordination by oxygen are highly stable in PdO_x–CeO_2 solid solutions.[53] The presence of atomic platinum as Pt^{2+} cations on ceria surfaces has been documented by several theoretical and experimental studies. Formation of these species was often related to the exposure of (100)-terminated facets.[22,23,54–56]

The present GGA+U data depend on the chosen U value. In particular, larger U values stabilize the presence of localized f electrons favoring processes that involve the reduction of Ce^{4+} to Ce^{3+}. To benchmark this dependence we calculated E_{ad} with different U values for a single Pd atom adsorbed on the $Ce_{40}O_{80}$ NP (see Fig. 4). The use of $U = 3$ eV decreases E_{ad} by 53 kJ mol^{-1} compared to that obtained with $U = 4$ eV chosen in this work. The use of a larger U value of 5 eV has an opposite effect on the E_{ad} increasing its magnitude by 54 kJ mol^{-1}. A similar trend was found for the binding of supported atomic Pt species on ceria.[22,57] In general, the usage of smaller, *i.e.* less interfering U values seems to be preferable. Yet, $U < 4$ eV values often do not allow complete localization of 4f electrons on the Ce^{3+} cations. The $U = 4$ eV employed throughout this work seems to be an adequate compromise providing a physically correct description of localized Ce 4f states and minimizing spurious stabilization of reduced Ce^{3+} species. One can also question, to what extent

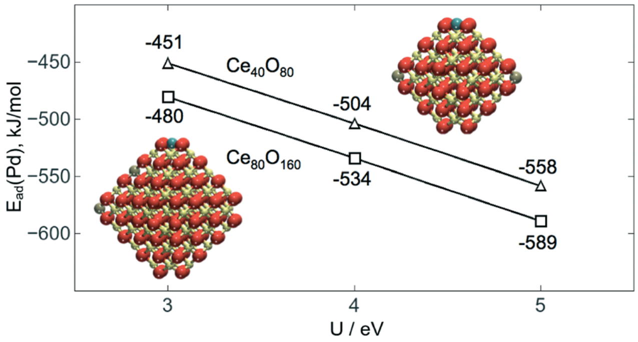

Fig. 4 Calculated adsorption energies E_{ad}(Pd) of single Pd atoms on the O_4 site of $Ce_{40}O_{80}$ and $Ce_{80}O_{160}$ NPs as a function of the *U* value used with the PW91 functional.

the O_4 site on the NP $Ce_{40}O_{80}$ represents the corresponding sites on other ceria nanostructures with similar surface terminations. Data in Fig. 4 shed light on this issue as well. Indeed, enlargement of the NP model to $Ce_{80}O_{160}$ (ref. 33 and 34) results in the strengthening of Pd–O_4 interactions by *ca.* 30 kJ mol^{-1}, implying that on larger ceria species transition metal atoms should be bound to the O_4 sites at least as strong as on the $Ce_{40}O_{80}$ model used in this study.

Group XI metals

Finally, adsorbed atoms of group XI, like those of group IX, exhibit several oxidation states. Moreover, each adsorbed group XI element can be in different oxidation states. The presence of Cu as Cu^{2+} ions in the ceria lattice was recently reported.[58] We calculated Cu^+ to be coordinated in a distorted linear fashion with two short (189 pm) and two long Cu–O distances (231 and 262 pm). Cu^{2+} adsorbs in a square-planar coordination mode with four equal Cu–O distances (199 pm). The Cu^{2+} state is found to be by 54 kJ mol^{-1} more stable than the Cu^+ state (Table 1). Atomic Ag can be adsorbed as either Ag^+ or Ag^{3+}, the latter was calculated to be somewhat more stable. The not very usual Ag^{3+} forms four Ag–O distances of 205–206 pm, in line with its square-planar coordination in oxoargentates.[59] Ag^+ is in a distorted square-planar coordination, where the metal atom is 90 pm above the O_4 plane. This distortion elongates Ag–O distances to 239–241 pm. Atomic Au can also be adsorbed as Au^+ and Au^{3+}, the latter being more stable by 70 kJ mol^{-1} (Table 1). Au, similar to the other presently investigated 5d metals, forms the highest oxidation state (+3) within the group. A linear coordination of Au^+ cations is preferred, with two short (206 pm) and two long distances (274 and 276 pm), while Au^{3+} prefers square-planar coordination (Au–O distances are 204–205 pm). Ag adsorbed as single atoms on microporous hollandite manganese oxide was found by XANES to feature the +1 oxidation state.[60] Meanwhile, gold can be stabilized both as Au^{3+} and Au^+ surface cations in ceria-supported gold catalysts.[61]

Table 1 Calculated adsorption energies E_{ad} and Bader charges *q* for atoms M adsorbed as M^{n+} cations on a $Ce_{40}O_{80}$ NP along with binding energies E_{ad79} of the M atoms on edges of M_{79} NPs (Fig. 2)

M	E_{ad}, kJ mol^{-1}	E_{ad79}, kJ mol^{-1}	$E_{ad79} - E_{ad}$, kJ mol^{-1}	*q*, au
Group VIII				
Fe^{3+}	−785	−630	155	1.50
Ru^{3+}	−812	−729	83	1.46
Os^{6+}	−978	−844	134	2.49
Group IX				
Co^{3+}	−709	−548	161	1.29
Rh^{2+}	−678	−612	66	1.07
Ir^{4+}	−830	−821	9	1.54
Group X				
Ni^{2+}	−678	−519	159	1.06
Pd^{2+}	−504	−377	127	0.91
Pt^{2+}	−678	−548	130	0.93
Group XI				
Cu^+	−412			0.73
Cu^{2+}	−466	−371	95	1.03
Ag^+	−277	−263	14	0.63
Ag^{3+}	−251			1.06
Au^+	−264			0.41
Au^{3+}	−334	−310	24	1.08

The adsorption energies in Table 1 reveal that the {100} nanofacet of ceria can strongly anchor not only atomic Pt, but other transition metal atoms as well. Furthermore, atoms of all considered transition metals are oxidized upon adsorption on the O_4 site. The Bader charges of adsorbed M_1 species reflect the formal oxidation states only qualitatively, being notably smaller than the latter and manifesting significant covalence in the M–O interactions. Despite the simplicity of the presently considered O_4 sites exposed by the $Ce_{40}O_{80}$ model NP, they are expected to be representative for a variety of experimental coordination environments of different transition metal cations. In particular, we are confident that our model NP allows us to quantify the strength of the M–O(–Ce) bonds formed by oxidized metal atoms. To assess whether these metal centers are resistant to agglomeration and sintering processes, which is a crucial issue in the design of metal-efficient SACs, one can compare the binding energies of transition metal atoms on the ceria NP surface and in the corresponding M_{79} NPs (Table 1).

For all M atoms under scrutiny, the adsorption energy E_{ad} on the ceria NP is larger in magnitude (more negative) than the binding energy E_{ad79} of an edge atom in the M_{79} NPs. This indicates that the metal dispersion as single atoms on the O_4 sites of ceria nanostructures is energetically favored over the formation of metallic particles. Therefore, very stable adsorption complexes on the nanoparticulate oxide support should resist sintering processes, especially for metals featuring substantial energy differences $\Delta E = E_{ad79} - E_{ad}$ (Table 1). The ΔE value defines the propensity of anchored metal atoms to form particles: the larger ΔE, the less prone the metal center is to sintering. We predict Fe^{3+}, Os^{6+}, Co^{3+} and group X metals to be particularly resistant to agglomeration in oxidative media. For group X metals, the extraordinary stability of the square-planar coordination for d^8 metal centers explains the particularly strong interaction with the ceria NP. Small ΔE values calculated for cationic Ag, Au, and Ir species suggest that these complexes are less resistant to sintering and might form metallic particles more readily. In order to further stabilize these metals as single atoms one should explore other supporting materials. Notably, the O_4 sites of CeO_2 nanostructures (not limited solely to $Ce_{40}O_{80}$ NPs) bind metal atoms notably more strongly than the extended $CeO_2(111)$ surface. For instance, the adsorption of Cu, Ag, and Au atoms on the latter surface resulted in PW91+3 E_{ad} values of −179, −96, and −69 kJ mol^{-1}, respectively.[62] This strongly suggests that the adsorption complexes of M_1 on {100} facets of CeO_2 NPs are substantially more resistant to agglomeration processes than on the $CeO_2(111)$ surface. It should be noted that since Pt was found to adsorb on both such surface and other non-{100} sites of the ceria NP with comparably low E_{ad},[22] other metals are expected to behave similarly.

Clear trends in calculated adsorption energies emerge along the rows and groups of the periodic table (Fig. 5). Both E_{ad} and E_{ad79} generally decrease in magnitude, when moving from the left to the right of the period. This indicates that metals with less occupied d bands form stronger metal–metal bonds and also bind more strongly to the oxide support. For 4d and 5d metals, such decreases in the E_{ad} and E_{ad79} are quite monotonous, with more pronounced differences for Au. The trend along the period for 3d metals is less linear and both E_{ad} and E_{ad79} values are crossed with those of the 4d and 5d metals. These trends also indicate that, except for Au, 5d metals form the strongest bonds with the O_4 site of the ceria NP, whereas 4d metals form the weakest bonds, with the exception of Ru.

The agglomeration of the transition metal content into the corresponding oxide phase under an oxidative environment would also lead to the destruction of the single-atom sites. Similar to sintering into metal NPs, the formation of the oxide phase would lead to less exposed metal atoms, with different properties and local environment. The propensity of the single-atom sites to such restructuring can be assessed from the experimental standard heats of formation (ΔH_f) for the most stable oxide phases of the metals under study (see Table S2†). In general, 3d metals are more prone to the formation of oxides than 4d and 5d metals, and the oxides of metals situated at the beginning of the period are more stable than those at the end of the period.[63] Comparing E_{ad} and ΔH_f values for each studied transition metal one expects generally high resistance against decomposition *via* the formation of a metal oxide phase except for Fe, which is quite susceptible to oxide formation.

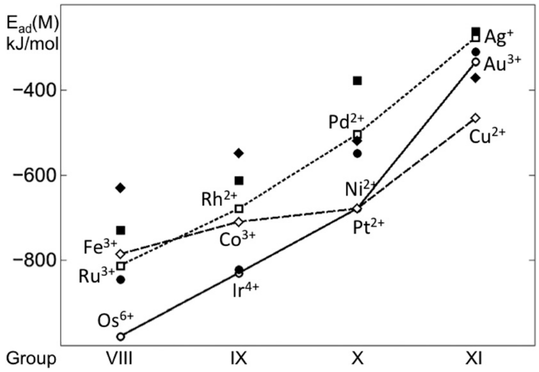

Fig. 5 Adsorption energies of single transition metal atoms (M) on the {100} facet of the $Ce_{40}O_{80}$ NP (empty points, connected as a guide) and binding energies of these atoms in edge positions of the M_{79} NP depicted in Fig. 2 (filled points). Results for 3d, 4d and 5d metals are shown by diamonds, squares, and circles, respectively.

All results of the present study correspond to stoichiometric ceria NPs, which are mostly relevant to conditions of ultra-high vacuum or very low oxygen pressure.[23] Yet, under ambient atmosphere and oxidative catalytic conditions ceria NPs can be stabilized by an excess of oxygen.[64–66] There, a variety of oxygen-containing surface species is expected to create a pool of additional adsorption sites capable of stabilizing oxidized transition metal atoms as potential SACs. We expect the binding properties of such sites to be quite similar to those of the sites on the {100} O-terminated facets of the stoichiometric NPs. This assumption is supported by the finding that oxygen atoms of the {100} O_4 sites are loosely bound to the ceria NPs,[33,34] which is reminiscent to the binding of the species adsorbed on the NP faces under excess O_2. Therefore, the present theoretical prediction that surface oxygen sites of nanostructured ceria are able to make diverse single-atom metal catalysts resistant to sintering probably can also be generalized to different experimental conditions.

The above results on the extreme stability of supported single metal atoms are expected to provide a guideline establishing suitable candidates for the design of SACs. This work opens a way to examine the catalytic function of the proposed materials individually for each reaction of interest. Co-sputtering of metals under an oxygen atmosphere, allowing the preparation of nanocomposites of atomically dispersed Pt on ceria,[22,67] can also be used to disperse other metals, the atoms of which are strongly bound to the square-planar O_4 sites. This has been demonstrated for model catalysts prepared according to the guidelines provided by the present calculations and comparing the stability and reactivity of Pt^{2+}, Pd^{2+}, and Ni^{2+} species on nanostructured ceria.[68] Interestingly, well-characterized steps on extended $CeO_2(111)$ surfaces[25,69] also appear to efficiently anchor Pt^{2+} by forming PtO_4 moieties, indicating that the preparation of ceria surfaces with very abundant steps also facilitates metal dispersion in the form of atoms.[70] In addition, the detailed structural data calculated in this work (*e.g.* metal coordination and metal–oxygen distances, see Fig. S1 and S2†) provide a benchmark for the characterization of atomically dispersed metal sites in SACs supported on CeO_2 NPs. For example, Pt coordination and Pt–O bond length measured by means of extended X-ray absorption fine structure (EXAFS)[54] experiments fully agree with the calculated structure of Pt^{2+} on the {100} sites of the ceria NPs.[22,23] Another implication of the present findings for nanocatalysis is related to the ability of some M_1–ceria SACs to undergo agglomeration and re-dispersion cycles under certain reaction conditions, forming metal clusters during the reaction and re-dispersing to the M_1–ceria state upon termination of the reaction.[71] The estimated stability $\Delta E = E_{ad79} - E_{ad}$ of the M_1–ceria materials with respect to the agglomeration in metal clusters (Table 1) controls that clusters remain small enough (possibly, subnano) and can readily transform back into single-atom species.

5. Summary

The interaction of 11 different transition metal atoms M = Fe, Ru, Os, Co, Rh, Ir, Ni, Pd, Cu, Ag, Au with the representative model $Ce_{40}O_{80}$ NP has been studied by means of GGA+U density-functional calculations. We have shown that adsorption sites of the ceria {100} nanofacets can very effectively anchor all considered metal atoms in the form of M^{n+} cations. The oxidation of the M centers takes place with the accompanying reduction of Ce^{4+} cations to Ce^{3+}. Calculated data indicate that higher oxidation states are favored by transition metals in later periods and in groups more to the left in the periodic table. The deposition of the M atoms leads to a significant structural reconstruction of the oxygen atoms constituting the adsorption site, which coordinate differently to the M^{n+} cation depending on its oxidation state. Remarkably, the adsorption for every M_1–ceria system studied is stronger than the binding of the corresponding M atom in a metal NP M_{79}. These adsorption energy differences are particularly large for the group X metals (Ni, Pd, and Pt) and for Fe, Co, and Os. This suggests that, especially for these metals, CeO_2-based materials exposing O_4 sites such as those on {100} nanofacets could provide suitable architectures for preparing single-metal atom catalysts with very high resistance to sintering. In general, the present calculated results are expected to be helpful in the preparation and atomic-level characterization of efficient single-atom catalysts, the limiting case in nanocatalysis featuring the smallest active species.

Acknowledgements

This work was financially supported by the European Community (FP7-NMP.2012.1.1-1 project ChipCAT, reference no. 310191), Spanish MINECO (grants CTQ2012-34969, CTQ2015-64618-R) and Generalitat de Catalunya (grants 2014SGR97 and XRQTC). The authors acknowledge a support by the COST Action CM1104 "Reducible oxide chemistry, structure and functions". Computer resources, technical expertise and assistance were provided by the Red Española de Supercomputación. We are grateful to Dr. Hristiyan Aleksandrov for his comments on the manuscript. AB acknowledges support from the European Research Council under the European Union's Seventh Framework Programme (FP/2007-2013) /Marie Curie Actions/grant no. 626764 (Nano-DeSign).

References

1 H. S. Gandhi, G. W. Graham and R. W. McCabe, *J. Catal.*, 2003, **216**, 433–442.
2 J. Tollefson, *Nature*, 2007, **450**, 334–335.
3 W. Vielstich, A. Lamm and H. A. Gasteiger, *Handbook of Fuel Cells: Fundamentals, Technology, Applications*, Wiley, Chichester, 2003.
4 W. R. Stamenkovic, B. S. Mun, M. Arenz, K. J. J. Mayrhofer, C. A. Lucas, G. F. Wang, P. N. Ross and N. M. Markovic, *Nat. Mater.*, 2007, **6**, 241–247.
5 H. T. Chung, J. H. Won and P. Zelenay, *Nat. Commun.*, 2013, **4**, 1922.
6 W. Yang, T.-P. Fellinger and M. Antonietti, *J. Am. Chem. Soc.*, 2011, **133**, 206–209.
7 A. Le Goff, V. Artero, B. Jousselme, P. D. Tran, N. Guillet, R. Métayé, A. Fihri, S. Palacin and M. Fontecave, *Science*, 2009, **326**, 1384–1387.
8 C. T. Campbell, *Acc. Chem. Res.*, 2013, **46**, 1712–1719.
9 R. Schlögl and S. B. Abd Hamid, *Angew. Chem., Int. Ed.*, 2004, **43**, 1628–1637.
10 M. Flytzani-Stephanopoulos and B. C. Gates, *Annu. Rev. Chem. Biomol. Eng.*, 2012, **3**, 545–574.
11 X.-F. Yang, A. Wang, B. Qiao, J. Li, J. Liu and T. Zhang, *Acc. Chem. Res.*, 2013, **46**, 1740–1748.
12 M. Flytzani-Stephanopoulos, *Acc. Chem. Res.*, 2014, **47**, 783–792.
13 K. M. Neyman, C. Inntam, V. A. Nasluzov, R. Kosarev and N. Rösch, *Appl. Phys. A: Mater. Sci. Process.*, 2004, **78**, 823–828.
14 A. Bruix, F. Nazari, K. M. Neyman and F. Illas, *J. Chem. Phys.*, 2011, **135**, 244708.
15 Q. Fu, H. Saltsburg and M. Flytzani-Stephanopoulos, *Science*, 2003, **301**, 935–938.
16 Y. P. Zhai, D. Pierre, R. Si, W. L. Deng, P. Ferrin, A. U. Nilekar, G. W. Peng, J. A. Herron, D. C. Bell, H. Saltsburg, M. Mavrikakis and M. Flytzani-Stephanopoulos, *Science*, 2010, **329**, 1633–1636.
17 M. Yang, S. Li, Y. Wang, J. A. Herron, Y. Xu, L. F. Allard, S. Lee, J. Huang, M. Mavrikakis and M. Flytzani-Stephanopoulos, *Science*, 2014, **346**, 1498–1501.
18 E. J. Peterson, A. T. DeLaRiva, S. Lin, R. S. Johnson, H. Guo, J. T. Miller, J. H. Kwak, C. H. F. Peden, B. Kiefer, L. F. Allard, F. H. Ribeiro and A. K. Datye, *Nat. Commun.*, 2014, **5**, 4885.
19 B. T. Qiao, A. Q. Wang, X. F. Yang, L. F. Allard, Z. Jiang, Y. T. Cui, J. Y. Liu, J. Li and T. Zhang, *Nat. Chem.*, 2011, **3**, 634–641.
20 G. Vilé, D. Albani, M. Nachtegaal, Z. Chen, D. Dontsova, M. Antonietti, N. López and J. Pérez-Ramírez, *Angew. Chem., Int. Ed.*, 2015, **54**, 11265–11269.
21 H. Wei, X. Liu, A. Wang, L. Zhang, B. Qiao, X. Yang, Y. Huang, S. Miao, J. Liu and T. Zhang, *Nat. Commun.*, 2014, **5**, 5634.
22 A. Bruix, Y. Lykhach, I. Matolínová, A. Neitzel, T. Skála, N. Tsud, M. Vorokhta, V. Stetsovych, K. Ševčíková, J. Mysliveček, R. Fiala, M. Václavů, K. C. Prince, S. Bruyère, V. Potin, F. Illas, V. Matolín, J. Libuda and K. M. Neyman, *Angew. Chem., Int. Ed.*, 2014, **53**, 10525–10530.
23 H. A. Aleksandrov, K. M. Neyman and G. N. Vayssilov, *Phys. Chem. Chem. Phys.*, 2015, **17**, 14551–14560.
24 Y. Pan, N. Nilius, C. Stiehler, H.-J. Freund, J. Goniakowski and C. Noguera, *Adv. Mater. Interfaces*, 2014, **1**, 1400404.

25 S. M. Kozlov, F. Viñes, N. Nilius, S. Shaikhutdinov and K. M. Neyman, *J. Phys. Chem. Lett.*, 2012, **3**, 1956–1961.

26 A. Hu, K. M. Neyman, M. Staufer, T. Belling, B. C. Gates and N. Rösch, *J. Am. Chem. Soc.*, 1999, **121**, 4522–4523.

27 V. I. Anisimov, F. Aryasetiawan and A. I. Lichtenstein, *J. Phys.: Condens. Matter*, 1997, **9**, 767–808.

28 V. I. Anisimov, I. V. Solovyev, M. A. Korotin, M. T. Czyzyk and G. A. Sawatzky, *Phys. Rev. B: Condens. Matter*, 1993, **48**, 16929–16934.

29 I. V. Solovyev, P. H. Dederichs and V. I. Anisimov, *Phys. Rev. B: Condens. Matter*, 1994, **50**, 16861–16871.

30 J. Paier, C. Penschke and J. Sauer, *Chem. Rev.*, 2013, **113**, 3949–3985.

31 C. Loschen, J. Carrasco, K. M. Neyman and F. Illas, *Phys. Rev. B: Condens. Matter*, 2007, **75**, 035115.

32 G. N. Vayssilov, A. Migani and K. Neyman, *J. Phys. Chem. C*, 2011, **115**, 16081–16086.

33 A. Migani, G. N. Vayssilov, S. T. Bromley, F. Illas and K. M. Neyman, *Chem. Commun.*, 2010, **46**, 5936–5938.

34 A. Migani, G. N. Vayssilov, S. T. Bromley, F. Illas and K. M. Neyman, *J. Mater. Chem.*, 2010, **20**, 10535–10546.

35 G. N. Vayssilov, Y. Lykhach, A. Migani, T. Staudt, G. P. Petrova, N. Tsud, T. Skála, A. Bruix, F. Illas, K. C. Prince, V. Matolín, K. M. Neyman and J. Libuda, *Nat. Mater.*, 2011, **10**, 310–315.

36 J. P. Perdew and Y. Wang, *Phys. Rev. B: Condens. Matter*, 1992, **45**, 13244–13249.

37 G. Kresse and J. Hafner, *Phys. Rev. B: Condens. Matter*, 1993, **47**, 558–561.

38 G. Kresse and J. Furthmüller, *Phys. Rev. B: Condens. Matter*, 1996, **54**, 11169–11186.

39 G. Kresse and J. Furthmüller, *Comput. Mater. Sci.*, 1996, **6**, 15–50.

40 P. E. Blöch, *Phys. Rev. B: Condens. Matter*, 1994, **50**, 17953–17979.

41 R. Bader, *Atoms in Molecules: A Quantum Theory*, Oxford University Press, USA, 1994.

42 M. M. Branda, R. M. Ferullo, M. Causà and F. Illas, *J. Phys. Chem. C*, 2011, **115**, 3716–3721.

43 H.-X. Mai, L.-D. Sun, Y.-W. Zhang, R. Si, W. Feng, H.-P. Zhang, H.-C. Liu and C.-H. Yan, *J. Phys. Chem. B*, 2005, **109**, 24380–24385.

44 A. Bruix, K. M. Neyman and F. Illas, *J. Phys. Chem. C*, 2010, **114**, 14202–14207.

45 M. A. Sk, S. M. Kozlov, K. H. Lim, A. Migani and K. M. Neyman, *J. Mater. Chem. A*, 2014, **2**, 18329–18338.

46 R. Nedyalkova, D. Niznansky and A.-C. Roger, *Catal. Commun.*, 2009, **10**, 1875–1880.

47 A. Satsuma, M. Yanagihara, J. Ohyama and K. Shimizu, *Catal. Today*, 2013, **201**, 62–67.

48 S. S.-Y. Lin, D. H. Kim, M. H. Engelhard and S. Y. Ha, *J. Catal.*, 2010, **273**, 229–235.

49 M. Haneda, K. Shinoda, A. Nagane, O. Houshito, H. Takagi, Y. Nakahara, K. Hiroe, T. Fujitani and H. Hamada, *J. Catal.*, 2008, **259**, 223–231.

50 Y. Huang, A. Wang, L. Li, X. Wang, D. Su and T. Zhang, *J. Catal.*, 2008, **255**, 144–152.

51 J. Carrasco, D. López-Durán, Z. Liu, T. Duchoň, J. Evans, S. D. Senanayake, E. J. Crumlin, V. Matolín, J. A. Rodríguez and M. V. Ganduglia-Pirovano, *Angew. Chem., Int. Ed.*, 2015, **54**, 3917–3921.

52 S. Colussi, A. Gayen, M. Farnesi Camellone, M. Boaro, J. Llorca, S. Fabris and A. Trovarelli, *Angew. Chem., Int. Ed.*, 2009, **48**, 8481–8484.

53 R. V. Gulyaev, T. Y. Kardash, S. E. Malykhin, O. A. Stonkus, A. S. Ivanova and A. I. Boronin, *Phys. Chem. Chem. Phys.*, 2014, **16**, 13523–13539.

54 Y. Nagai, T. Hirabayashi, K. Dohmae, N. Takagi, T. Minami, H. Shinjoh and S. Matsumoto, *J. Catal.*, 2006, **242**, 103–109.

55 T. Wu, X. Pan, Y. Zhang, Z. Miao, B. Zhang, J. Li and X. Yang, *J. Phys. Chem. Lett.*, 2014, **5**, 2479–2483.

56 Y. Gao, W. Wang, S. Chang and W. Huang, *ChemCatChem*, 2013, **5**, 3610–3620.

57 A. Bruix, A. Migani, G. N. Vayssilov, K. M. Neyman, J. Libuda and F. Illas, *Phys. Chem. Chem. Phys.*, 2011, **13**, 11384–11392.

58 J. S. Elias, M. Risch, L. Giordano, A. N. Mansour and Y. Shao-Horn, *J. Am. Chem. Soc.*, 2014, **136**, 17193–17200.

59 H. Müller-Buschbaum, *Z. Anorg. Allg. Chem.*, 2004, **630**, 2125–2175.

60 P. Hu, Z. Huang, Z. Amghouz, M. Makkee, F. Xu, F. Kapteijn, A. Dikhtiarenko, Y. Chen, X. Gu and X. Tang, *Angew. Chem., Int. Ed.*, 2014, **53**, 3418–3421.

61 A. M. Venezia, G. Pantaleo, A. Longo, G. Di Carlo, M. P. Casaletto, F. L. Liotta and G. Deganello, *J. Phys. Chem. B*, 2005, **109**, 2821–2827.

62 M. M. Branda, N. C. Hernández, J. F. Sanz and F. Illas, *J. Phys. Chem. C*, 2010, **114**, 1934–1941.

63 D. F. Shriver and P. W. Atkins, *Inorganic Chemistry*, Oxford University Press, 3rd edn, 1999.

64 G. Preda, A. Migani, K. M. Neyman, S. T. Bromley, F. Illas and G. Pacchioni, *J. Phys. Chem. C*, 2011, **115**, 5817–5822.

65 J. Kullgren, K. Hermansson and P. Broqvist, *J. Phys. Chem. Lett.*, 2013, **4**, 604–608.

66 X. Huang and M. Beck, *Chem. Mater.*, 2015, **27**, 2965–2972.

67 R. Fiala, A. Figueroba, A. Bruix, M. Václavů, A. Rednyk, I. Khalakhan, M. Vorokhta, J. Lavková, F. Illas, V. Potin, I. Matolínová, K. M. Neyman and V. Matolín, *Appl. Catal., B*, 2016, DOI: 10.1016/j.apcatb.2016.02.036.

68 A. Neitzel, A. Figueroba, Y. Lykhach, T. Skála, M. Vorokhta, N. Tsud, S. Mehl, K. Sevciková, K. C. Prince, K. M. Neyman, V. Matolín and J. Libuda, submitted.

69 N. Nilius, S. M. Kozlov, J.-F. Jerratsch, M. Baron, X. Shao, F. Viñes, S. Shaikhutdinov, K. M. Neyman and H.-J. Freund, *ACS Nano*, 2012, **6**, 1126–1133.

70 F. Dvořák, M. Farnesi Camellone, A. Tovt, N.-D. Tran, F. R. Negreiros, M. Vorokhta, T. Skála, I. Matolínová, J. Mysliveček, V. Matolín and S. Fabris, *Nat. Commun.*, 2016, 7, 10801.

71 M. Hatanaka, N. Takahashi, N. Takahashi, T. Tanabe, Y. Nagai, A. Suda and H. Shinjoh, *J. Catal.*, 2009, **266**, 182–190.